

An effective coaxiality error measurement for twist drill based on line structured light sensor

Ailing Cheng¹, Jiaojiao Ye², Fei Yang², Shufang Lu¹, Fei Gao¹

¹ College of Computer Science and Technology, Zhejiang University of Technology, Hangzhou 310023, China

² Research Center of Intelligent Computing Software, Zhejiang Lab, Hangzhou 311121, China

Abstract— Since the structure of twist drill is complex, it is hard and challenging for its coaxiality error measurement. In this paper, a novel mechanism, framework and method of coaxiality error measurement for twist drill is proposed. The mechanism includes encoder, PLC controller, line structured sensor and high precision turntable. First, profile point cloud data of the twist drill is collected through the line structured light sensor when the drill turns around in the controlling of PLC. Second, a GMM-based point cloud segmentation algorithm based on local depth features is investigated to extract blade back data. To improve the measurement accuracy, a statistical filter is designed to remove outliers during the target region extraction. Then, according to two characteristics of coaxiality error, an axis reconstruction method based on orthogonal synthesis of axisymmetric contour differences is presented, which is facilitated to pre-position the maximum deviation cross sections of the drill axis. Finally, the coaxiality error is measured through fitting the benchmark axis and the axis at the pre-positioned maximum deviation position. At the end, a large number of experiments are carried out, and it shows that our method is accuracy and robust.

Note to Practitioners— This article studies a coaxiality error measurement method for twist drill. Due to the complexity of twist drill in shape, it is hard and challenging to obtain accurate cross section circle data of twist drill efficiently and calculate the coaxiality error. In this article, an effective mechanism and framework is proposed to measure coaxiality error for twist drill, and a robust segmentation method is designed to extract blade back which is on cross section circle. Furthermore, a maximum axis deviation location method is proposed to reduce the amount of calculation. Experimental results show that the presented method is precise and effective, and performs noticeably well than the existing approaches. Moreover, the proposed framework performs well in solving coaxiality error measurement for workpieces with complex surface, and the maximum axis deviation location method behaves well in dealing with the problem of data loss.

Index Terms—coaxiality error measurement, twist drill, line structured light sensor, Gaussian Mixture Model, point cloud segmentation

I. INTRODUCTION

Coaxiality error is a common form and position tolerance in the mechanical product testing [1][2]. Traditionally,

combination device of v-type bracket, steel ball plus lever dial gauge or yaw meter is a familiar contact measurement tool [3][4][5] in the industry. Relatively, Coordinate Measuring Machine (CMM) [1][6][7][8] is more precise and stable, but it is time-consuming when the sampling number increases. On the other hand, non-contact method based on optics has attracted plentiful attentions, which can be classified into two types: active non-contact method and passive non-contact method. Stereo-vision [9][10][11][12][13] achieves the measurement through 3D reconstruction, which is a passive non-contact method and is simple and fast. However, this method depends much more on the richness of the surface texture and the accuracy is usually low. Although Phase-shifting interferometry [14] is a high accuracy method is widely used in modern measurements, the accuracy is sensitive to environment technique is compact measurement method and is suitable for factors like vibration and temperature. Time-of-flight (TOF) mobile applications [15][16], of which the precision is not very favorable. Structured light technique [17][18][19] utilizes projecting light with certain structured patterns for 3D reconstruction and measurement. The patterns can usually be spot, strip, plane or specially customized using different bands of spectrum. Numerous codification methods have been researched with some being discussed by Salvi et al. [18]. Among them, line structured light technology has been especially concerned due to its high frequency and flexible application.

Generally, line structured light technology acquires point cloud of objects, and processes them to achieve particular geometric sense. One of the core steps is to extract the key region, i.e. point cloud segmentation (PCS), which is one of the hotspots in the point cloud field. Usually, PCS is achieved by using the key 3D geometric information together with some constraints and statistical rules according to different point cloud format. Current PCS methods can be classified into four types as follows [20][21][22]: edge-based method, region-growing method, model-fitting method, and clustering-based method.

Principle of the edge-based method is to detect the changes of the density or depth of edge points, of which the basis is that object shape can be described by edges. Sometimes, 3D point cloud data are transferred to 2D image. Sappa et al. [23] proposed a two-stage segmentation approach by utilizing scan line approximation to quickly process very large range images,

which includes binary map generation and counter detection. Wani et al. [24] sliced 3D image to create depth contours and extracted three types of pixels and edges from the various EDCs. Huang et al. [25] proposed a systematic approach to automatically extract geometric surface features from a point cloud composed of a set of unorganized three-dimensional coordinate points by data segmentation.

Region-growing method combines characteristics from two region elements or two points to measure the resemblances among points or voxels and merges them. According to whether or not an initial seed will be set, current researches can be summarized as two branches, i.e. seed region method and non-seed region method. Deschaud et al. [26] proposed a voxel-based region-growing algorithm to enhance efficiency by replacing points with voxels during region growing operation. Vo et al. [27] presented an accommodative octree-based region-growing algorithm for fast surface patch segmentation by incrementally merging adjacent voxels with a similar saliency characteristics. These methods are properly classical and fast, it is especially effective on regular scenarios. However, they cannot take a good performance when data is not sufficient or excessive.

The core idea of model-fitting method is that point cloud data is matched with different original geometric primitives. Hough Transform (HT) and Random Sample Consensus (RANSAC) are two of the most classical algorithms. Hulik et al. [28] advised a plane detection method based on 3D Hough transformation. In the method, continuous frame data accumulation and iteration were used to achieve the segmentation of the plane. Nurunnabi et al. [29] put forward a statistical technique for outliers detection in point cloud data to achieve robust plane segmentation in laser scanning data. At present, RANSAC is widely used and is derived into many variants [20].

Clustering-based methods are composed of a mixture of different approaches that own a similar target, i.e. the point cloud data are segmented by clustering similar points in spectral features, geometric features, or spatial distribution. Early k-means [30][31], mean shift [32][33] and fuzzy clustering [34] are the mainstream algorithms. Besides, feature similarity measures like Euclidean distance, density, normal vector and so on attract many attentions [35]. In contrast to region-growing method and model-fitting method, there is no pre-definition in the clustering-based method [20][21], which is widely used in the segmentation of irregular and complex objects. In addition, deep learning based on PCS has been extensively researched and applied on different data formatting [22]. Nevertheless, little efforts are paid on point cloud data segmentation based on line structured light sensor since it has different feature mode [22].

Other core question around the measurement based on line structured light sensor is how to design a proper measurement mode, namely, how to obtain objects the 3D information precisely and efficiently. Similar to roundness, radial jump variable and radius, coaxiality error is a kind of geometric tolerances. As shown in Fig. 1, it is defined as the diameter of minimum envelope cylinder structured by actual axis deviating from reference axis. Many efforts are paid on form and position tolerance measurements. For example, Chai et al. [36] proposed a method based on laser displacement sensor for coaxiality error

measurement of composite gear by obtaining cross-sectional contours, separating apex data on gears and fitting the center of the cross section. Pei et al. [37] utilized single laser displacement sensor to realize radial jump variable measurement of gears, which improved the measurement accuracy by optimizing laser angle and installation position. Li et al. [38] used laser displacement sensors to obtain surface profile of a part and fitted the center of the circle to calculate the concentricity of large forging, so as to improve the operation accuracy of disassembly and assembly. Liang et al. [39] presented a non-contact measurement prototype based on a laser displacement sensor for automatic evaluation of rolling performance of spline shaft.

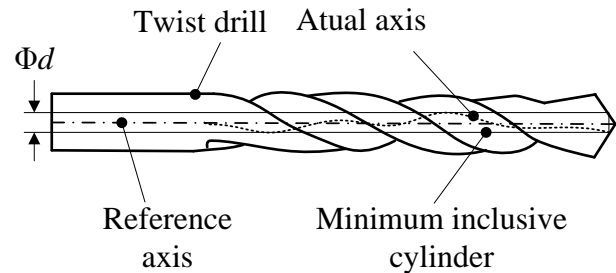


Fig. 1. Illustration of coaxiality error for twist drill.

Twist drill is an axial complex-faced work piece. It is challenging for its coaxiality error measurement. According to the aforementioned analysis of current literatures, there are still some limitations as follows: 1) The whole 3D information needs to be captured, which is time-consuming, 2) little method is suitable for coaxiality error measurement of objects with complex surface like twist drill, and 3) it is difficult for current methods to achieve the coaxiality error measurement when the point cloud data is insufficient or missing.

To overcome the aforementioned limitations, a novel mechanism, framework and method of coaxiality error measurement for twist drill is proposed. Through data analysis of drill cross section, GMM and EM are employed to implement the point cloud segmentation of blade back. It can properly solve problem 2). During the phase of axis calculation, a method that combines differences of two axisymmetric profiles and orthogonal synthesis is proposed to determine the maximum axis deviation location and the offset. It gives an intuitive location estimation through curves simulation of two groups of axisymmetric profiles. Compare with curve fitting method, this method only utilizes a small number of profiles and can greatly reduce the influence of data lack. It solves the problem 1) large calculation and 3) data insufficiency. Meanwhile, this method can simultaneously calculate the maximum axis deviation location and deviation amount whether if the point data is intact. The main contributions are as follows:

- (1) A framework and method of coaxiality error measurement for twist drill is proposed, which includes such modules as system calibration, target region extraction, axis maximum deviation location and coaxiality error calculation. The framework and method can intuitively measure the coaxiality error of workpieces with complex surfaces and insufficient data.
- (2) A blade back extraction method based on local depth features of GMM is put forward to extract target point data of complex surfaces.

(3) An axis reconstruction method based on orthogonal synthesis of axisymmetric contours differences is presented, which is novel, simple and effect.

(4) A mechanism of coaxiality error measurement for twist drill is developed, which integrates the proposed framework and method.

This paper first describes a coaxiality error measurement

framework based on 3D reconstruction, details data acquisition and system calibration. And then the relevant key technologies were discussed. After that, the accuracy of the measurement framework was verified and analyzed. Finally, the research direction and development trend were analyzed.

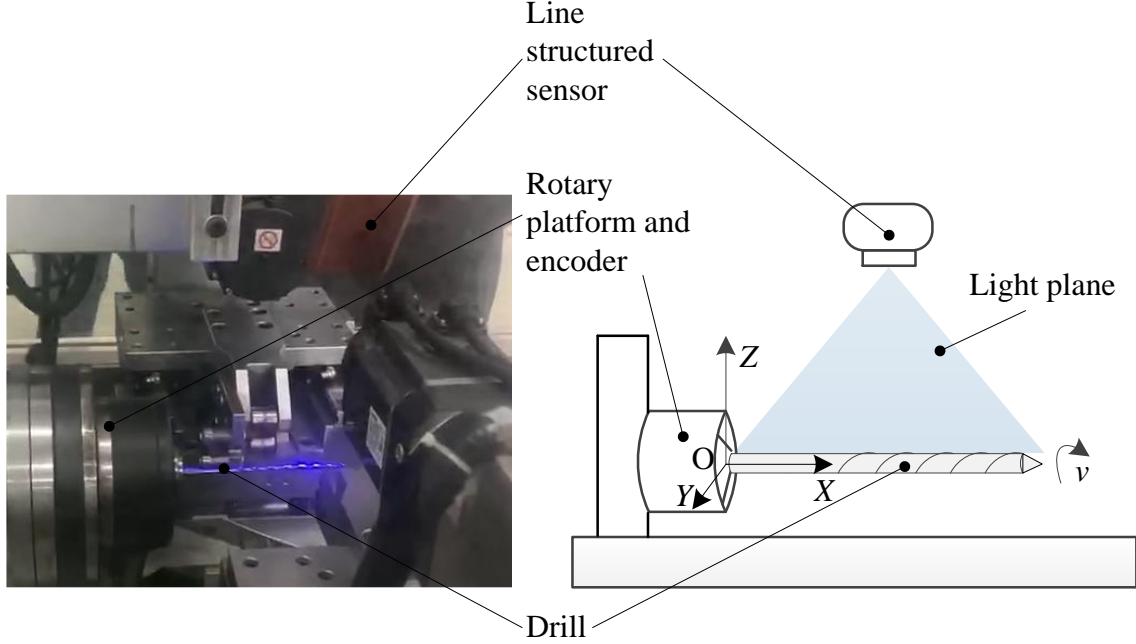


Fig. 2. Coaxiality Error Measurement Equipment for Twist Drill.

II. MECHANISM

A. Components and principle

To improve the efficiency and accuracy of coaxiality error measurement for twist drill, a mechanism based on 3D measurement is designed, as shown in Fig. 2. The mechanism comprises several main components such as PLC, differential encoder, line structured light sensor and high-precision turntable. Among them, the turntable drives drills to run around turntable axis in command of PLC, meanwhile differential encoder acquires sequential angle signals and triggers line structured light sensor to catch point cloud data of drill surface, which are the core principle of the mechanism. On this basis, raw data is collected for target region extraction and other algorithms processing.

B. Data acquisition

In the data acquisition phase, the drill is grasped and rotates around turntable axis in command of PLC, differential encoder acquires sequential rotation signals from the turntable, and triggers the sensor to catch point cloud data of continuous contours on the drill surface. During the process, any i -th sampled point data, $P_i = \{i, x_{ij}, z_{ij}\}$, in the sensor coordinate system after rotating θ degree can be transformed to a 3-D point data $P'_i = \{x'_{ij}, y'_{ij}, z'_{ij}\}$ in the measurement coordinate system, where, $i=1, 2, \dots, I, j=1, 2, \dots, J, I$ is the sensor triggered times, J is the point cloud number of a single sampling, as shown in Fig. 3. When the rotation reaches a cycle, the turntable is

commanded to stop by PLC and the coaxiality error calculation officially begins.

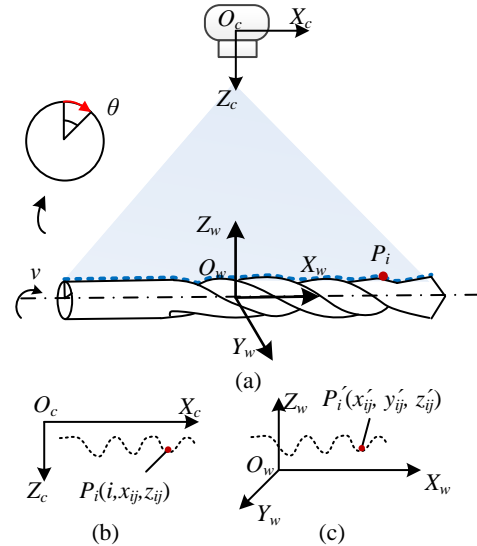


Fig. 3. (a) Illustration of point cloud collection. (b) Point cloud in sensor coordinate system. (c) Point cloud in measurement coordinate system. P'_i corresponds to P_i .

C. Coordinate transformation

As shown in Fig. 4, in the measurement system, $O_c X_c Y_c Z_c$ is the sensor coordinate system and $O_w X_w Y_w Z_w$ is the measurement coordinate system. The conversion from sensor coordinate system to measurement coordinate system is according to Eq. (1):

$$\begin{cases} \theta_i = \frac{360^\circ}{I} * i \\ x'_{ij} = x_{ij} \\ y'_{ij} = (D - z_{ij}) * \sin \theta_i \\ z'_{ij} = (D - z_{ij}) * \cos \theta_i \end{cases} \quad (1)$$

Where, $i=1, 2, \dots, I$, I indicates the times that the sensor is triggered, $j=1, 2, \dots, J$, J is the number of point clouds for a single frame contour. x_{ij} and z_{ij} are point cloud data acquired by line structured light sensor after rotating θ_i degree.

x'_{ij} , y'_{ij} and z'_{ij} are the transformed data corresponding x_{ij} , z_{ij} and θ_i . D is the distance from the sensor to the axis of the turntable, which is the system parameter and needed to be calibrated.

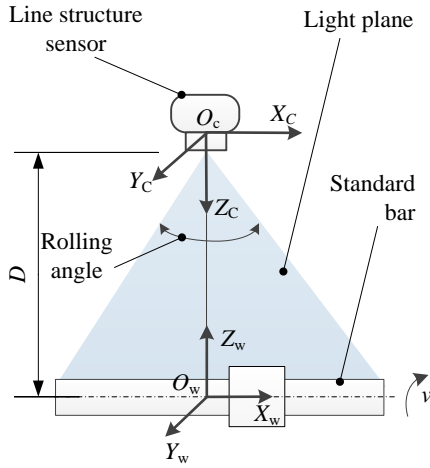


Fig. 4. Relationship between sensor coordinate and measurement coordinate. $O_c X_c Y_c Z_c$ is the sensor coordinate system and $O_w X_w Y_w Z_w$ is the measurement coordinate system.

D. Calibration and adjustment

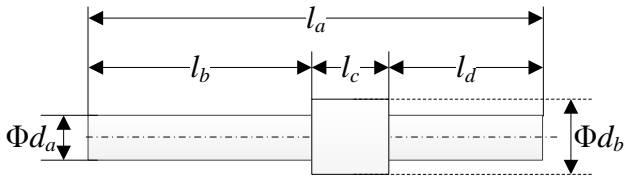


Fig. 5. Calibration block diagram.

To determine the system parameter D , a calibration block with a stepped shaft is designed to calibrate the system as shown in Fig. 5. Purpose of the design of ladder is as follows: since surface of a drill twined by spiral grooves may not be scanned completely according to the optical measurement constraints of line structured light sensor based on triangulation, the ladder can make contribution to sensor installation that a relatively perfect posture and position can be achieved by referring to the ladder. The sensor pose can be described by Euler angles including pitching angle, yawing angle and rolling angle. In the measurement system, as shown in Fig. 4, rolling angle, pitching angle and yaw angle are respectively corresponding to the rotation around $O_w Y_w$, $O_w X_w$ and $O_w Z_w$ axes. Therefore, the system calibration not only aims to determine D but also provide the guide for the mechanism installation to achieve high-precision measure effect.

According to the adjustment and calibration rules from coarse to fine, a cyclic adjustment method based on three degrees of freedom is proposed. Detailedly, in the mechanism installation, pose and installation position of the sensor are continuously being fine-tuned according to installation height, rolling angle and the position on $O_w Y_w$ axis until it meets RULE I, II and III.

RULE I. The calibration block appears completely in the field of sensor view.

RULE II. The outline of the calibration block is close to a straight line and satisfies Eq. (2).

$$\begin{cases} x_b - x_a = x_c - x_b = x_d - x_c \\ \Delta z = |z_d - z_a| \\ \Delta z \leq \Delta z_{th} \end{cases} \quad (2)$$

Where, as shown in Fig. 6(a), (x_a, z_a) , (x_b, z_b) , (x_c, z_c) and (x_d, z_d) are the coordinates of P_A , P_B , P_C and P_D collected by the sensor, respectively. P_B and P_C are the two endpoints of the ladder. Δz_{th} is the line threshold given by experience and is usually set to be less than 3 times z resolution.

RULE III. Fine-tune Position of the sensor on the $O_w Y_w$ axis is fine-tuned. As shown in Fig. 6(b), for the points P_B and P_C on the calibration block, a series points data can be acquired and be recorded as two sets, i.e. $\{i, x_{Bi}, z_{Bi}\}$ and $\{i, x_{Ci}, z_{Ci}\}$ for P_B and P_C , respectively. When the data satisfying Eq. (3):

$$\begin{cases} z_{Bi} + z_{Ci} < z_{B(i-1)} + z_{C(i-1)} \\ z_{Bi} + z_{Ci} < z_{B(i+1)} + z_{C(i+1)} \end{cases} \quad (3)$$

At this time, the sensor position on the $O_w Y_w$ axis is the best, that is, the sensor is closest to the calibration block, and i is denoted as i^* . Then system parameter D can be obtained from Eq. (4):

$$D = \min(z_{B i^*} + z_{C i^*}) / 2 \quad (4)$$

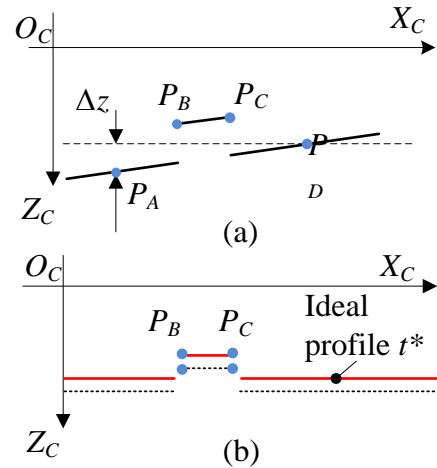


Fig. 6. Schematic diagram of calibration block contour. (a) is the situation in criterion I but not II and III. The red line in (b) is the situation in criterion I, II and III. P_A , P_B , P_C and P_D are evenly axial spaced point, P_B and P_C are the two endpoints of the ladder

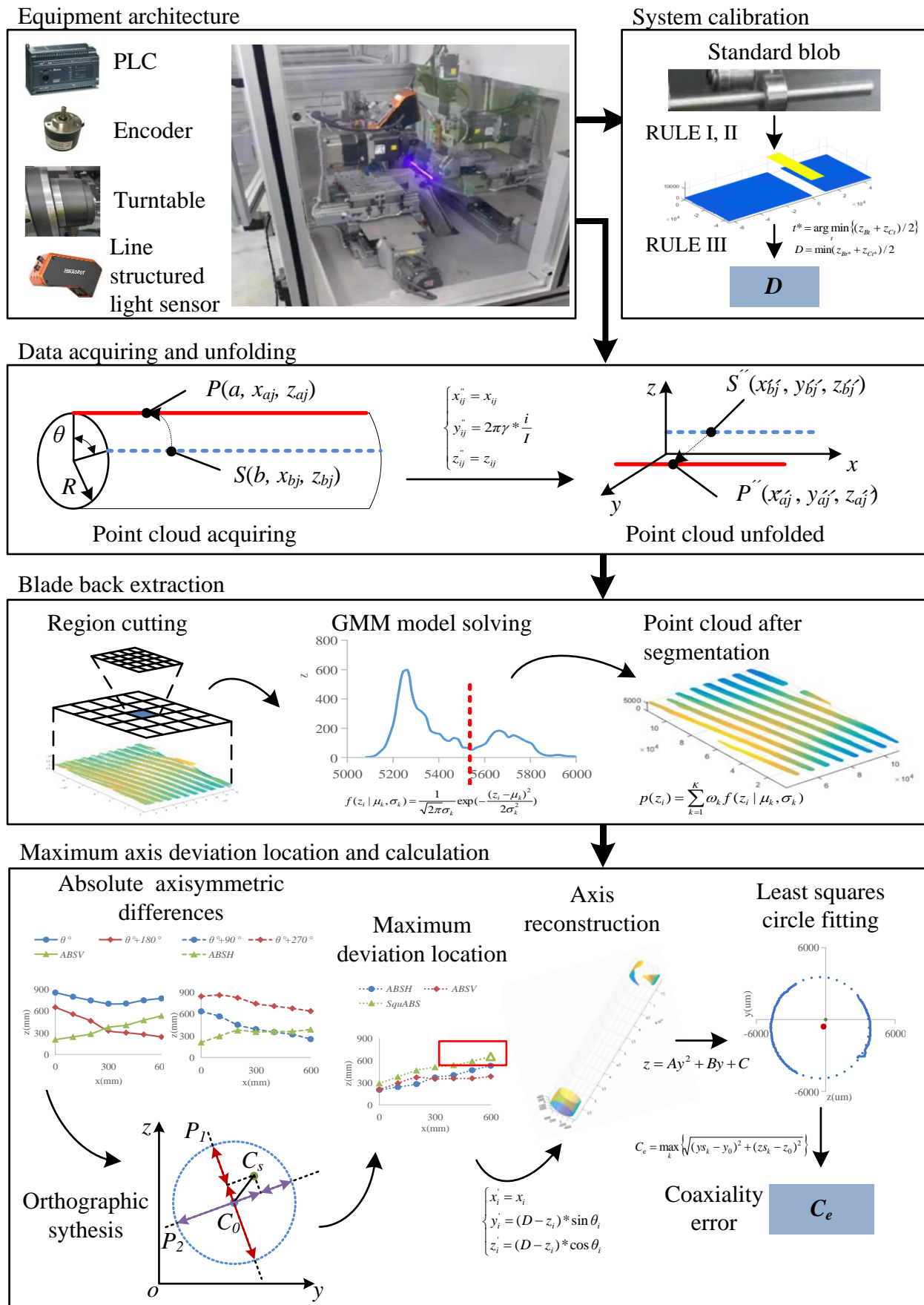


Fig. 7. Flow chart of measurement framework.

III. FRAMEWORK AND METHOD

The framework of the coaxiality error measurement is shown in Fig. 7.

A. Point cloud transformation and preprocessing

Point cloud transformation provides a convenient data model for target region extracting. As shown in Fig. 8, S and P are the points respectively collected at the a -th and b -th time, S'' and P'' are the transformed points, which are calculated according to Eq. (5).

$$\begin{cases} x_{ij}'' = x_{ij} \\ y_{ij}'' = 2\pi\gamma * \frac{i}{I} \\ z_{ij}'' = z_{ij} \end{cases} \quad (5)$$

Where, γ is the transformation coefficient and is given manually. $i=1, 2, \dots, I, j=1, 2, \dots, J$. i is the number of times that the sensor was triggered. J is the point clouds number of a single sampling. $\{i, x_{ij}, z_{ij}\}$ is the i -th sampled point data set in the sensor coordinate system, and $\{x_{ij}'', y_{ij}'', z_{ij}''\}$ is the corresponding transformed data set. Since there may be noises in the data acquisition process, a straight-through filter is used to perform basic outlier removal.

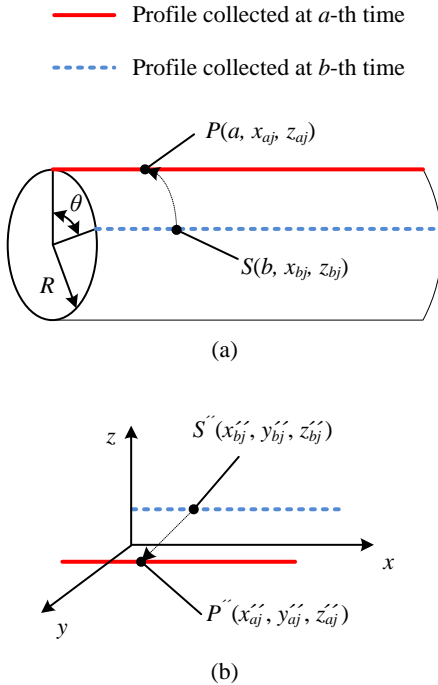


Fig. 8. Point cloud transformation. (a) Point cloud before transformation. (b) Point cloud after the transformation. S and P are points respectively collected at the a -th and b -th time sampling. S'' and P'' are the points corresponding to S and P after the transformation respectively

B. Blade back extraction

Blade back extraction aims to segment point clouds lying on standard circle from the perspective of cross section for coaxiality error calculation. According to the analysis of drill geometry characteristics and the collected data, a GMM-based point cloud segmentation method based on local depth features

is proposed to extract target regions, where, there are two steps as follows: 1) mathematical modeling on the profile point cloud data is carried out according to the principle that different contour segments belong to different sub-models, 2) GMM and EM are used to split point cloud by solving model parameters and membership probability to extract the desired regions. Meanwhile, in the process of solving the model, to comply with the law of large numbers, an idea of local region is introduced to avoid wrong segmentation caused by axis deviation. Furthermore, to better facilitate the model of blade back extraction in the actual applications, two rules, i.e. RULE IV and V, are advised:

RULE IV. Target point clouds lying on each cross section must be located on the circle.

RULE V. Each class of point clouds lying on the axial profiles must satisfy its own independent identical distribution.

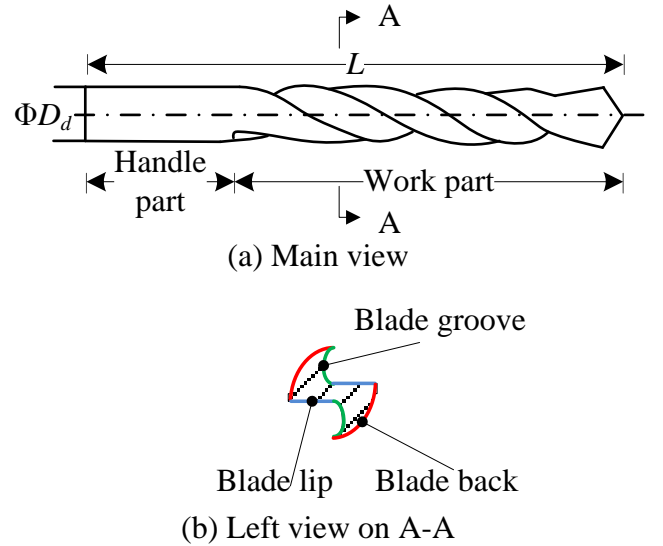


Fig. 9. Geometric figure of twist drill. Blade back is red, blade lip is blue, blade groove is green.

1) Analysis of target region selection

The purpose of region selection is to determine the point clouds of what regions can be included in the coaxiality error measurement. The profile of a drill on cross section is mainly composed of three parts, i.e. blade back, blade lip and blade groove, which are marked in red, blue and green respectively as shown in Fig. 9. The contour formed by the blade back on the cross section is located on a circle, which meets RULE IV. On the other hand, the measurement based on line structured light sensor is achieved by capturing the light reflected from surfaces of the measuring objects. Then, three constraints must be satisfied as follows: 1) measuring points must be located within the camera's depth of field range (DOF), 2) measuring points are within the field of camera vision (FOV), and 3) the angle between the reflected light of the measuring point and its surface normal vector must be less than the incident angle. During the scanning process based on the rotation measurement, only the whole of blade back, part of blade lip and no blade groove can be scanned due to the shape characteristics of twist drill and the limitation of optical constraints, as shown in Fig. 10 (blue lines for blade back, red

lines for blade lip and few part of blade groove). Therefore, point clouds of a drill for one scanning period is shown in the Fig. 11 (a). Any two-dimensional axial contour data like the black line in the Fig. 11 (a) is shown in Fig. 11 (b). z value of the point clouds presents a ladder distribution, where the upper part represents the blade lip and the lower part represents the blade back. The statistical histogram of point cloud depth values in a certain region can be obtained as shown in Fig. 11 (c). The depth values of point clouds jointly constitute a Gaussian mixture distribution, which meets independent identical distribution. So, it satisfies RULE V.

Light plane

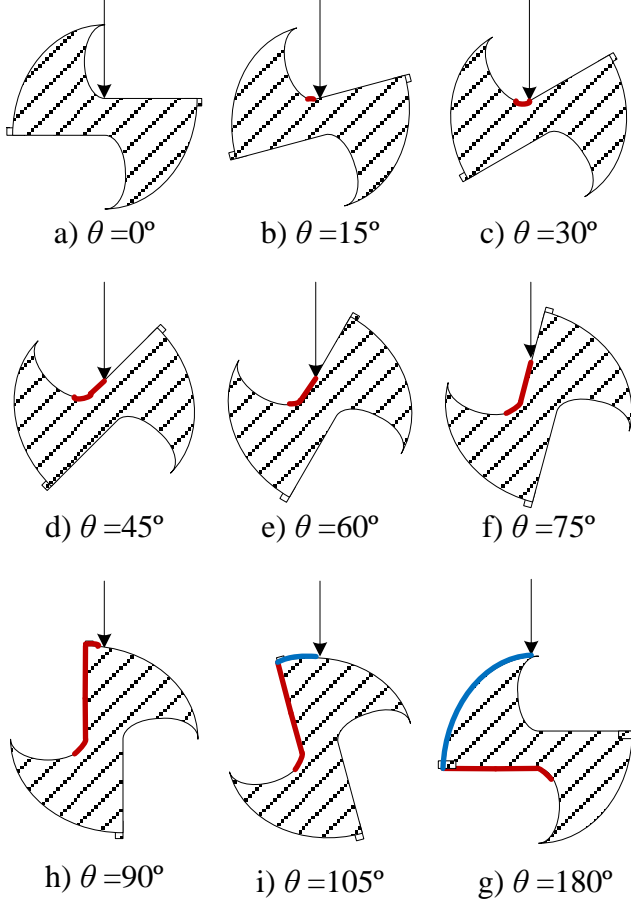


Fig. 10. Scanning process of drill cross section after certain rotation angle. Blue line is for blade back, red line is for blade lip and few parts of blade groove.

2) Mathematical model building

In the GMM, point clouds of blade back are defined as the foreground and others are selected as the background. So, Eq. (6~8) are satisfied for any z_i , $i=1, 2, \dots, N$, where, N is the number of point clouds.

$$p(z_i) = \sum_{k=1}^K \omega_k f(z_i | \mu_k, \sigma_k) \quad (6)$$

$$\sum_{k=1}^K \omega_k = 1 \quad (7)$$

$$f(z_i | \mu_k, \sigma_k) = \frac{1}{\sqrt{2\pi}\sigma_k} \exp\left(-\frac{(z_i - \mu_k)^2}{2\sigma_k^2}\right) \quad (8)$$

Where, $k = 1, 2, \dots, K$, K is the number of categories in the GMM. $p(z)$ is the joint probability density function of z . μ_k and σ_k are the expectation and the standard deviation of the k -th Gaussian distribution, ω_k is the weight of each Gaussian distribution in the model, f is the probability density function of z .

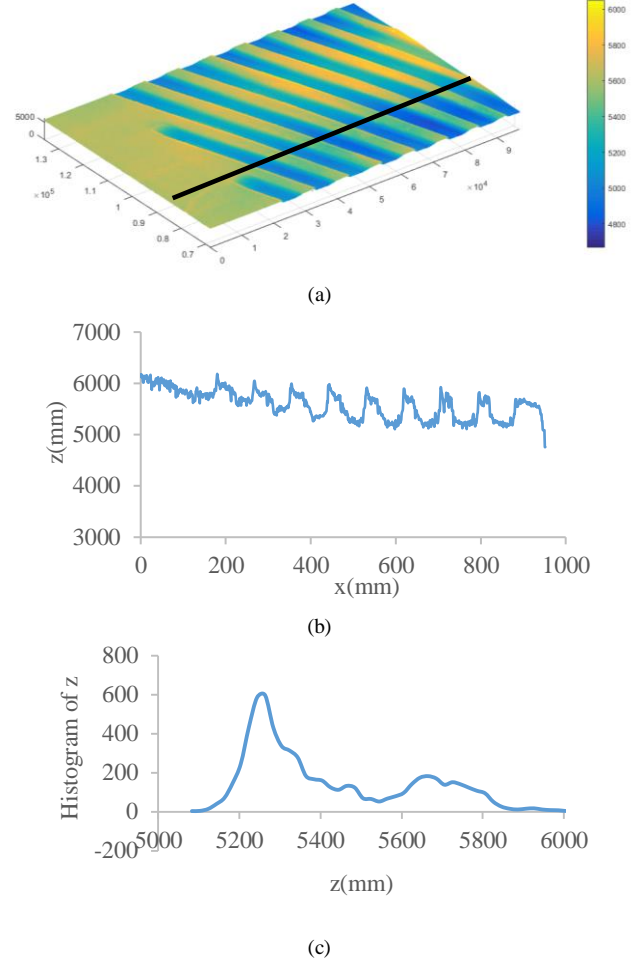


Fig. 11. (a) Point cloud of a drill. (b) The 2-D x and z profile data on black line in (a). (c) Histogram of z of a certain region on work part in (a).

In this way, point cloud segmentation is transformed into GMM-based classification, but it is unknown for model parameters and probability density function. Usually, the expect-maximum (EM) algorithm based on iterative optimization strategy can be employed to solve the problem. To obtain a good convergence effect, there will be certain requirements for parameter initialization, iteration times and termination conditions.

The proposed GMM-based point cloud segmentation method is based on local depth features. Two levels of divisions are carried out on the transformed point cloud. First, point clouds are parted into several blocks. GMM is applied for every block. Second, blocks are evenly divided into certain number of patches. Maximum frequency of Z value within every patch is affirmed to be the depth value of the patch and

elected to join in the GMM and EM calculation. Steps of the proposed method are as follows:

1) Point clouds are equally divided into $M*N*T$ blocks along the three axes, i.e. O_cX_c , O_cY_c and O_cZ_c , to obtain the blocks set $B, b_i \in B, i=1, 2, \dots, M*N*T$. M, N and T are the number of blocks along the O_cX_c , O_cY_c and O_cZ_c axes respectively. T is set as 1.

2) Blocks are evenly divided into $m*n*t$ patches along the three axes, i.e. O_cX_c , O_cY_c and O_cZ_c , to obtain the patches set $F, f_j \in F, j=1, 2, \dots, m*n*t$. m, n and t are the number of patches along the O_cX_c , O_cY_c and O_cZ_c axes respectively. t is set as 1.

3) The histogram the depth value of every patch, $h_j(z)$, is calculated and the highest frequency value, zf_j , can be calculated according to Eq. (9), K is the number of point clouds within a patch f_j :

$$zf_j = \arg \max_{z_k} \{h(z)\}, k = 1, 2, \dots, K \quad (9)$$

4) Initialization parameters of EM is calculated according to Eq. (10):

$$\begin{cases} FA = \sum_{j=1}^{m*n*t} zf_j \\ FMax = \max\{zf_j\} \\ FMin = \min\{zf_j\} \\ \sigma_F = \sigma_B = (FMax - FMin) / 4 \\ \mu_F = FA - \sigma_F \\ \mu_B = FA + \sigma_B \end{cases} \quad (10)$$

Where, FA , $FMax$ and $FMin$ are the mean, maximum and minimum value of the z -coordinate of patches within a block, respectively. μ_F , σ_F , μ_B and σ_B are the expectation and standard deviation of GMM corresponding to the foreground and background respectively. Both ω_F and ω_B in Eq. (6) and (7) are set to be 0.5.

5) EM is employed to solve the model with the aforementioned given values of the parameters of the GMM.

In the proposed method, the result may be affected by the block size to a certain extent. According to the experience, the segmentation performs best if the block size is approximately close to the sum of a single blade back and blade lip, and it is verified in the experiments. The reason is that when the block size is taken like that, the distribution difference between the blade back and blade lip is most obvious, and the model is more convenient for convergence. Furthermore, a statistical filter SOR is utilized for filtering the segmented point clouds in consideration of the inevitable noise, which is described in the experiments in detail.

C. Coaxiality error calculation

Coaxiality error measurement is to calculate the maximum radial distance from actual axis to reference axis. The computing overhead will be greatly reduced if the maximum deviation location is pre-estimated in advance. Hence, a novel axis reconstruction method based on orthogonal synthesis of axisymmetric contours difference is proposed. In the method, maximum deviation position of the axis is pre-positioned by using the extracted blade back data and the approximately

reconstructed axis. The basis are the two characteristics of coaxiality error, i.e. coaxiality error is proportional to the opposite phase differences and neighboring phase differences are independent to each other. The so-called opposite phase difference is the absolute difference between any two axisymmetric profiles, which is proportional to the coaxiality error. The so-called neighboring phase differences mean any two orthogonal axisymmetric profiles differences. They are independent to each other on impacting the coaxiality error. So reversely, coaxiality error can be orthogonal synthesized by any two orthogonal axisymmetric profiles differences, which will be described in the following section in detail.

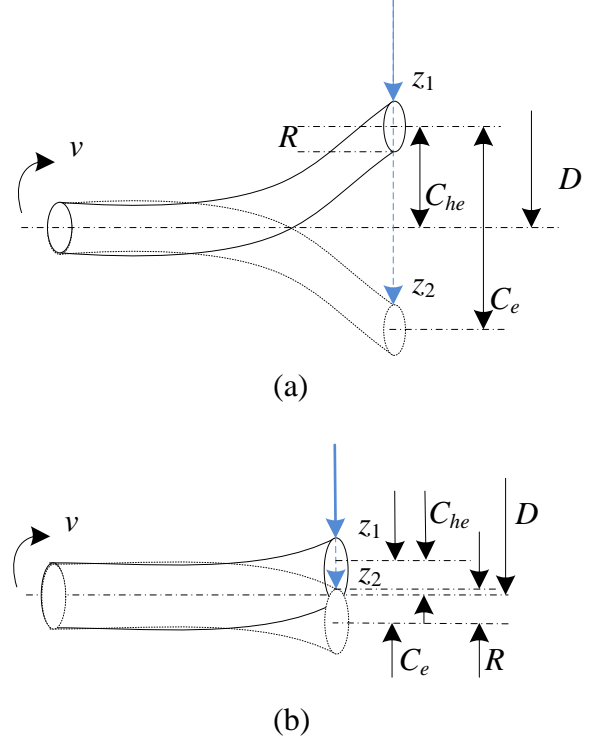


Fig. 12. Coaxiality error approximate axisymmetric difference illustration. (a) Coaxiality error is less than the diameter of the measured object. (b) Conditions of otherwise (a).

1) Analysis of axis deviation

As for an object with good roundness and coaxiality, during the rotation around its axis, absolute depth difference between the axial contour under any angle θ and its axisymmetric contour at $\theta+180^\circ$ is approximately 0. When the coaxiality error increases, the contrast difference improves. Two cases of coaxiality error in vivo and not in vivo are illustrated in Fig. 12 respectively. R is the radius of twist drill, C_e is the coaxiality error and C_{he} is half of C_e . In the Fig. 12(a), z_1 and z_2 are respectively the depth values of the same measuring points at any rotation angle of the drill θ and $\theta+180^\circ$, respectively, which satisfies Eq. (11) and (12).

$$z_1 \approx D - R - 0.5 * C_e \quad (11)$$

$$z_2 \approx D + (0.5 * C_e - R) \quad (12)$$

Eq. (13) can be obtained according to Eq. (11) and (12):

$$C_e \approx z_2 - z_1 \quad (13)$$

Similarly, the situation in the Fig. 12(b) satisfies Eq. (14) and (15).

$$z_1 \approx D - (R + 0.5 * C_e) \quad (14)$$

$$z_2 \approx D - (R - 0.5 * C_e) \quad (15)$$

Then, Eq. (16) can be also obtained according to Eq. (14) and (15).

$$C_e \approx z_2 - z_1 \quad (16)$$

It can be seen from Eq. (13) and (16) that the depth value at any point on the drill is directly proportional to absolute value of the difference between its depth value and axisymmetric position. Therefore, axisymmetric difference can directly reflect the size of coaxiality error.

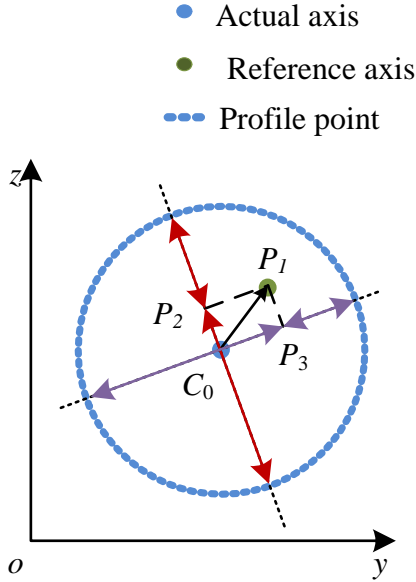


Fig. 13. Orthogonal decomposition and synthesis of coaxiality errors.

In other words, coaxiality error can be orthogonal synthesis by two orthogonal axisymmetric profiles differences. As shown in Fig. 13, P_1 is the reference axis and C_0 is the actual axis. For any group of orthogonal directions, $\vec{C_0P_2}$ and $\vec{C_0P_3}$, the axial center deviation $\vec{C_0P_1}$ can be generated by orthogonal synthesis, which satisfies Eq. (16).

$$|\vec{C_0P_1}| = \sqrt{|\vec{C_0P_2}|^2 + |\vec{C_0P_3}|^2} \quad (16)$$

2) Location and calculation of maximum axis deviation

In the maximum axis deviation location phase, the key step is to select two sets of orthogonal axisymmetric contours point clouds, and establish mathematical description model by utilizing quadratic spline to fit those contours, and then, the approximate actual axis contour is constructed by using orthogonal synthesis, after that the maximum axis deviation positions are located. In the quadratic spline fitting, the median depth value of each sub-connected region is used to calculate the node parameters of the spline functions. The specific algorithm is as follows:

- 1) Two groups of orthogonal axisymmetric profiles are selected to contribute a point clouds set $C_i = \{x_{ik}, z_{ik}\}$, $k=1, 2, \dots, K$, K denotes the number of point clouds on every profile. $i=1, 2, 3, 4$, i corresponds $\theta, \theta+90^\circ, \theta+180^\circ$ and $\theta+270^\circ$ angle.
- 2) Quadratic spline functions of the selected profiles are constructed by utilizing the extracted point data.

3) The absolute differences of every two axisymmetric are calculated, the absolute difference of θ and $\theta+180^\circ$ are named as $ABSV$, the other two is denoted as $ABSH$, $ABSV = \{x_{hk}, z_{vk}\}$ and $ABSH = \{x_{hk}, z_{hk}\}$, which are calculated according to Eq. (17) and (18).

$$\begin{cases} x_{hk} = x_{0k} = x_{2k} \\ z_{hk} = |z_{0k} - z_{2k}| \end{cases} \quad (17)$$

$$\begin{cases} x_{vk} = x_{1k} = x_{3k} \\ z_{vk} = |z_{1k} - z_{3k}| \end{cases} \quad (18)$$

4) The approximate axis deviation profile is reconstructed by utilizing Eq. (19) and is denoted as $SquABS = \{xs_k, zs_k\}$.

$$\begin{cases} xs_k = x_{hk} = x_{vk} \\ zs_k = \sqrt{z_{hk}^2 + z_{vk}^2} \end{cases} \quad (19)$$

5) The maximum axis deviation position is located by using Eq. (20). To reduce the location error, a threshold Δzs is set, and the zs_k of points that satisfies $zs_k > zs_{max} - \Delta zs$ is gathered to form a set $XSM = \{xsm_t | t=1, 2, \dots, T\}$, T is the pre-positioned number of cross sections. XSM includes the located positions:

$$xs_{max} = \arg \max(zs_k), k=1, 2, \dots, K \quad (20)$$

6) In the located set XSM , Eq. (1) is used to convert the point clouds into those in the measurement coordinate system, and circular least-square circle method is used to fit the cross-section point clouds, according to Eq. (21). Then, the fitted axis coordinates (ys, zs) and the radius R can be obtained according to Eq. (22):

$$z = Ay^2 + By + C \quad (21)$$

$$\begin{cases} ys = -A / 2 \\ zs = -B / 2 \\ R = 0.5 * \sqrt{A^2 + B^2 - 4C} \end{cases} \quad (22)$$

The same method is used to calculate the reference axis, i.e. the axis of the drill handle, to get the reference coordinates (Y_0, Z_0). Then, the coaxiality error C_e is the maximum deviation of the circle center within the located positions range, which is calculated according to Eq. (23).

$$C_e = 2 * \max_t \left\{ \sqrt{(ys_t - y_0)^2 + (zs_t - z_0)^2} \right\} \quad (23)$$

Where, $t=1, 2, \dots, T$, T is the number of located maximum deviation positions.

IV. EXPERIMENT AND DISCUSSION

A. Setup

The experimental point clouds were collected by a line structured light sensor named MV-DP090-02B. For the convenience of calculation, a region of interest is set up for the sensor, which makes that a single profile includes 1350 points. The specific parameters of the sensor are shown in Table I. Encoder is differential and the parameters of the turntable are detailed in Table II. In addition, the point cloud processing was

performed on a computer with the windows 7, i7 CPU and memory 8G using a point cloud framework PCL1.8.1.

Table I
MV-DP090-02B parameters

Parameter	Value
Single contour points	1920
Measurement range (X-axis (width))-near side (mm)	80
Measurement range (X-axis (width))-far side (mm)	153
Measurement range (Z-axis (height))-near side (mm)	106.5
Measurement range (Z-axis (height))-far side (mm)	200.0
Resolution (X-axis) (mm)	0.042~0.080
Resolution (Z-axis) (mm)	0.013~0.047
Repetition precision (Z-axis)(um)	3
Scanning frequency (Hz)	60~1000

Table II
Turntable parameters

Parameter	Value
Angle resolution	0.001°
Repeated positioning accuracy	0.002°
Eccentric(um)	5

Line structured
sensor

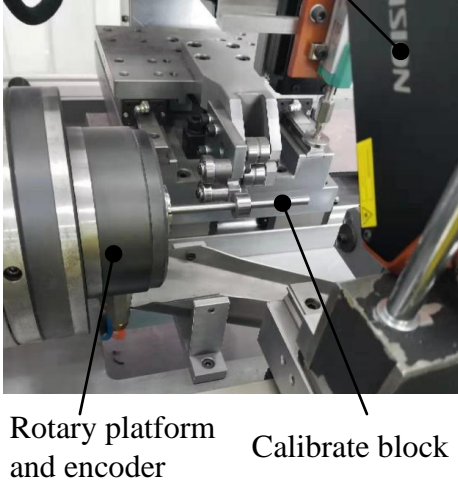


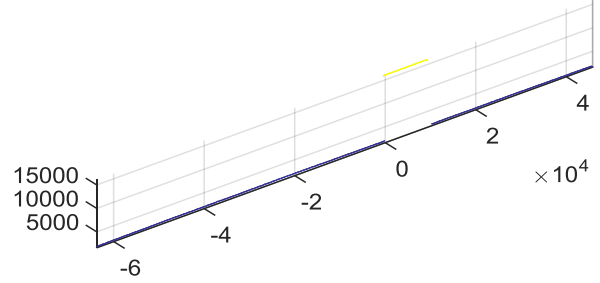
Fig. 14. The calibration of measuring equipment.

B. System calibration

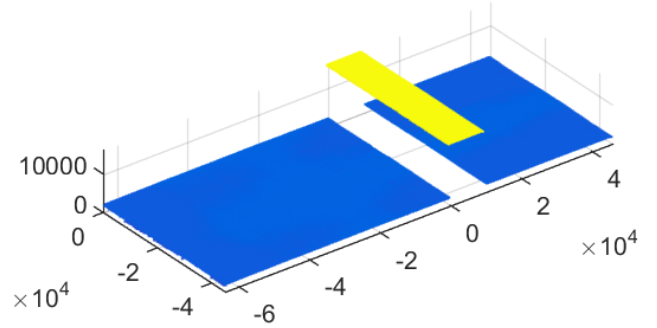
A customized calibration block as shown in Table III is machined with accuracy 2um. Firstly, the device is fixed and adjusted to make the calibration block merge in the field of the line structured sensor vision, as shown in Fig. 14. Secondly, roll angle of the sensor is adjusted to make that the light plane of the sensor is parallel to the axis of the calibration block, and Δz_{th} in Eq. (3) is set to be 1 um. Then the position of the sensor in the Y-axis direction is fine-tuned to let to be closest to the camera. By now the optimal installation position is reached, z_{Bi} and z_{Ci} is measured and parameter D can be obtained. The profile of calibration block reaching RULE II is shown in Fig. 15(a). The point cloud of calibration block for one revolution is as shown in Fig. 15 (b).

Table III
The calibration block parameter

Parameter	Value
$l_a(\text{mm})$	120
$l_b(\text{mm})$	70
$l_c(\text{mm})$	10
$l_d(\text{mm})$	40
$\Phi d_a(\text{mm})$	8
$\Phi d_b(\text{mm})$	14



(a)



(b)

Fig. 15. Calibration effect diagram. (a) The profile of calibration block reaching RULE II. (b) The cloud points of calibration block reaching RULE III.

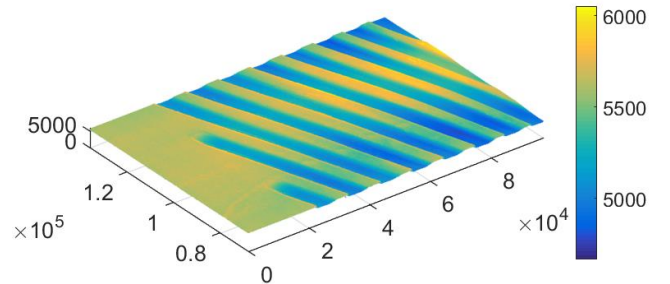


Fig. 16. Point cloud transformed.

C. Analysis of blade back extraction

The transformed point cloud data is shown in Fig. 16. In the phase of the GMM model solution, initialization parameters (such as: μ_F , σ_F , ω_F , μ_B , σ_B , ω_B) and the local region size both have certain influence on segmentation effect. An ocean of experiments were carried out and showed that the best performance were achieved when initialization parameters were set as Eq. (10) and the local size was close to the sum of single blade back and blade lip about 10 mm for 8 mm diameter and 100 mm length drills. The reason is that when the block size is taken as such, the distribution difference between blade back and blade lip is the most obvious, the model is more convenient for convergence. Besides, the local size can be predicted by advanced estimation. Segmentation results of different size are shown in Fig. 17.

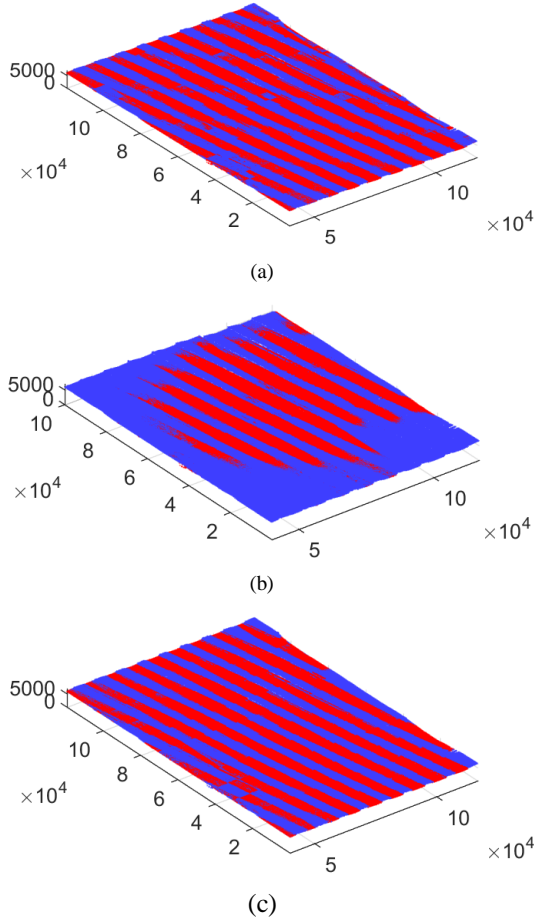


Fig. 17. Comparison of different size of regions in Gaussian mixture model before filter. (a) $M=N=5$ mm. (b) $M=N=40$ mm. (c) $M=N=10$ mm (The best size)

There are noise and wrong classed points existing in the segmented regions, for that a statistical filter is designed and applied in after point cloud processing. The comparison effects before and after statistical filter are shown in Fig. 18.

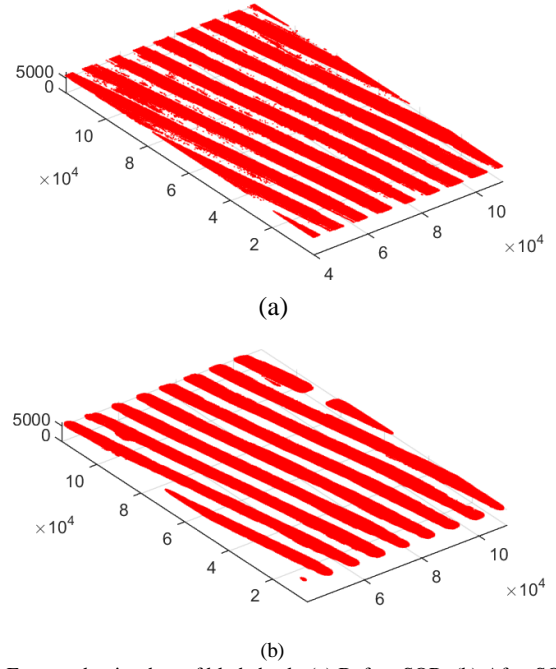


Fig. 18. Extracted point data of blade back. (a) Before SOR. (b) After SOR.

In addition, considering the complexity of the drill surface, in order to achieve more precise segmentation, other algorithms are also attempted for comparative analysis, such as Region Growing (RG), Conditional Euclidean Distance (CE) and Model Based (MB). RG method was assuming blade back area as a plane, selected seeds randomly and took the normal vector threshold of neighborhood as the termination condition. CE method combined the intensity, normal vector and point cloud depth for extracting blade back region. MB method utilized point clouds of drills to create model of the profiles and recognized the blade back. Different results are shown as in Fig. 19.

As can be seen from Fig. 19, our method achieved the best segmentation effect. Due to rough and reflective surface of drills, MB method occurred large probability deviation in the estimation of the splines. Similarly, RG showed dreadful ability because of small differences between normal vectors owing to optics constraints. CE get the worst result.

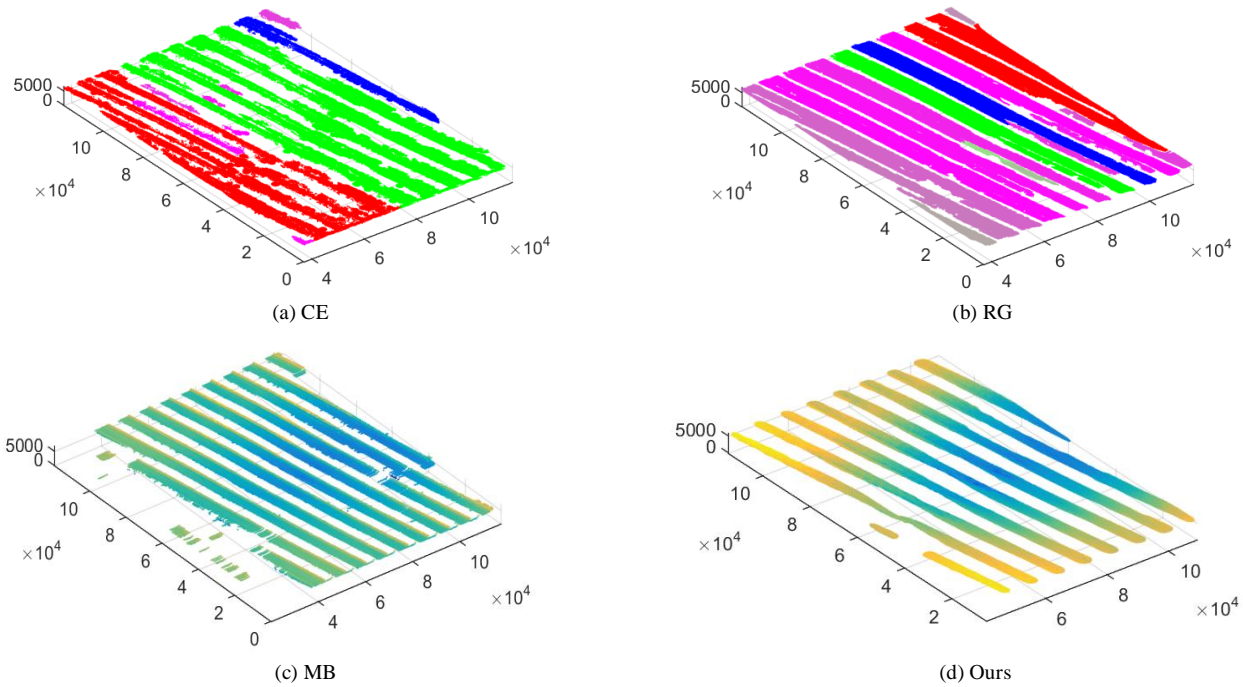


Fig. 19. The different point cloud segmentation comparison.

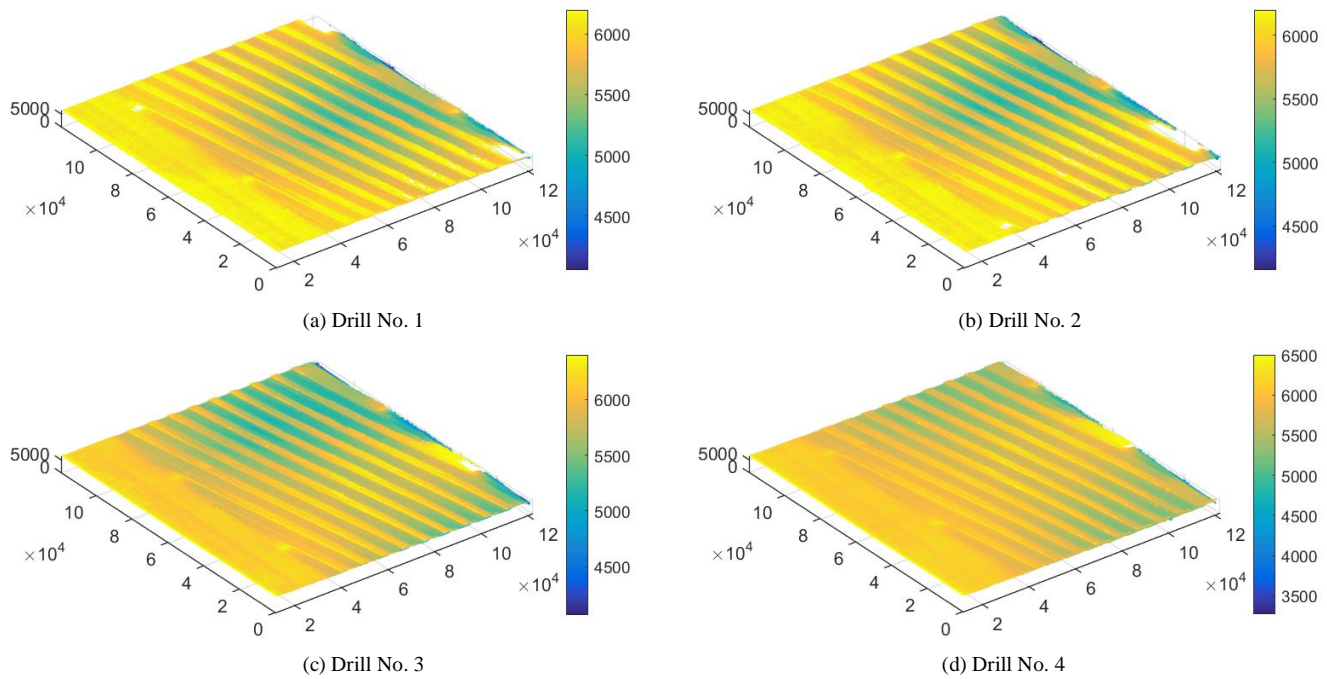
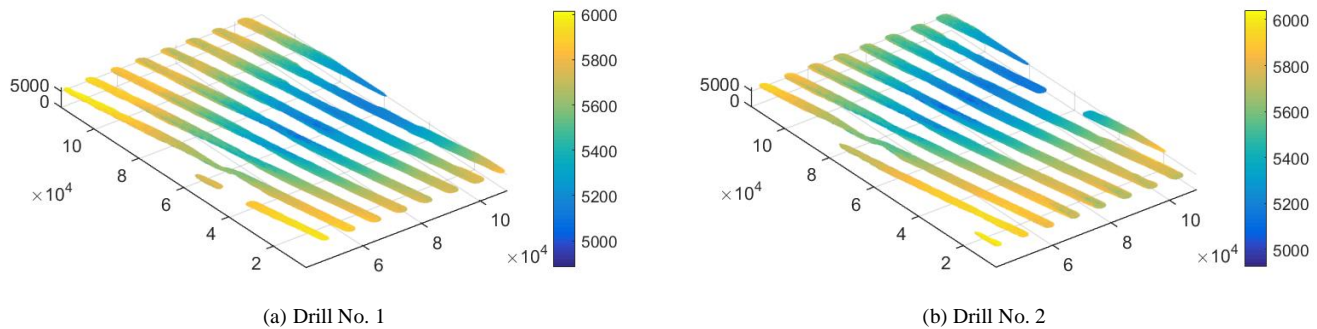
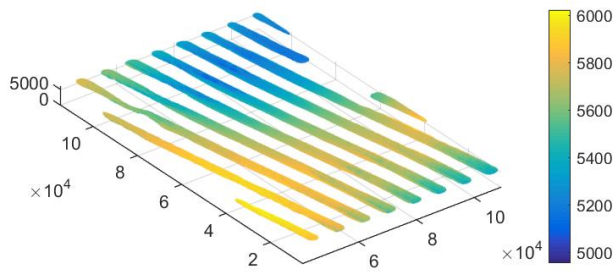
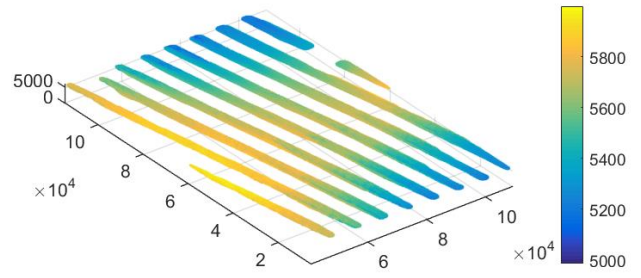


Fig. 20. Point cloud of Drill No.1~4 with different bending degree.





(c) Drill No. 3



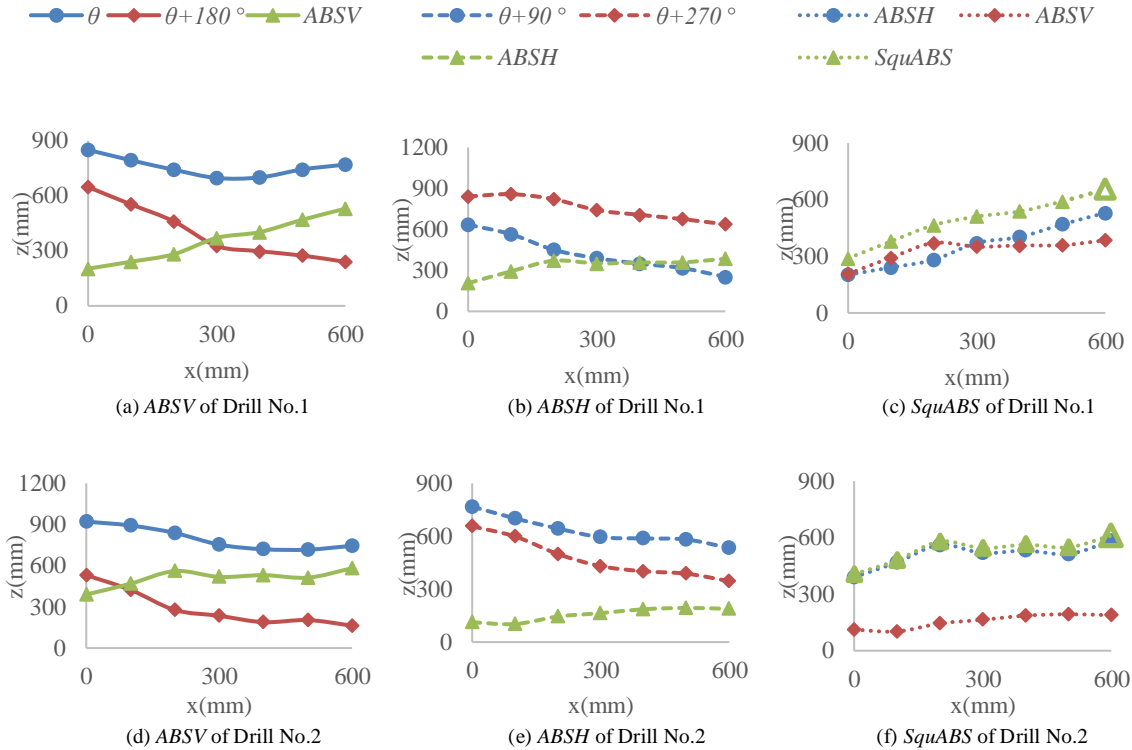
(d) Drill No. 4

Fig. 21. Point cloud of blade back.

D. Analysis of maximum axis deviation location and calculation

Axis maximum deviation location utilizes orthogonal synthesis from two sets absolute differences of axisymmetric profiles differences to reconstruct actual axis contour. For illustrating the experiment, four drills with different bending degree are presented here as shown in Fig. 20. Point clouds after blade back extraction is shown in Fig. 21. A group of contour lines were randomly selected within the point cloud of blade back, and the angles were respectively θ , $\theta+90^\circ$, $\theta+180^\circ$ and $\theta+270^\circ$. According to axis maximum deviation location method defined in section 3.3.2, the absolute difference value $ABSV$ between θ and $\theta+180^\circ$ and $ABSH$

between $\theta+90^\circ$ and $\theta+270^\circ$ were calculated respectively, as shown in Fig. 22(a)(b)(d)(e)(g)(h)(j)(k). Then the actual axis of drills is approximately constructed by using orthogonal synthesis, as shown in Fig. 22(c)(f)(i)(l). As can be seen from Fig. 22(c)(f)(i)(l), when two pairs of axisymmetric profiles differences are nearly the same, the axis deviation after orthogonal synthesis is larger than both of them, as shown in Fig. 22(c) and (l) hollow Δ is the position of the maximum axis deviation. When two pairs of axisymmetric profiles differences differ largely, the axis after orthogonal synthesis is closer to the larger one as shown in Fig. 22(f) and (i), hollow Δ is the position with the largest axis deviations. That is obeying relevant rules of orthogonal synthesis.



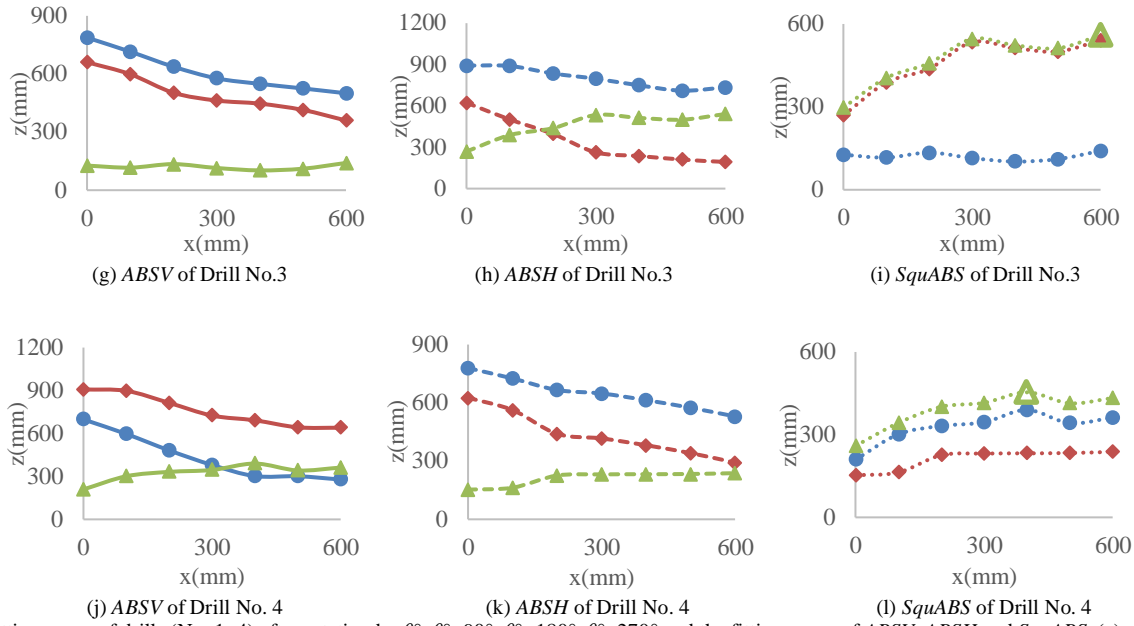


Fig. 22. The fitting curve of drills (No. 1~4) after rotating by θ° , $\theta^\circ+90^\circ$, $\theta^\circ+180^\circ$, $\theta^\circ+270^\circ$ and the fitting curve of ABSV, ABSH and SquABS. (a)~(c) are the profiles of drill No. 1. (d)~(f) are the profiles of drill No. 2. (g)~(i) are the profiles of drill No. 3. (j)~(l) are the profiles of drill No. 4. Hollow triangle Δ is the predicted maximum axis deviation position.

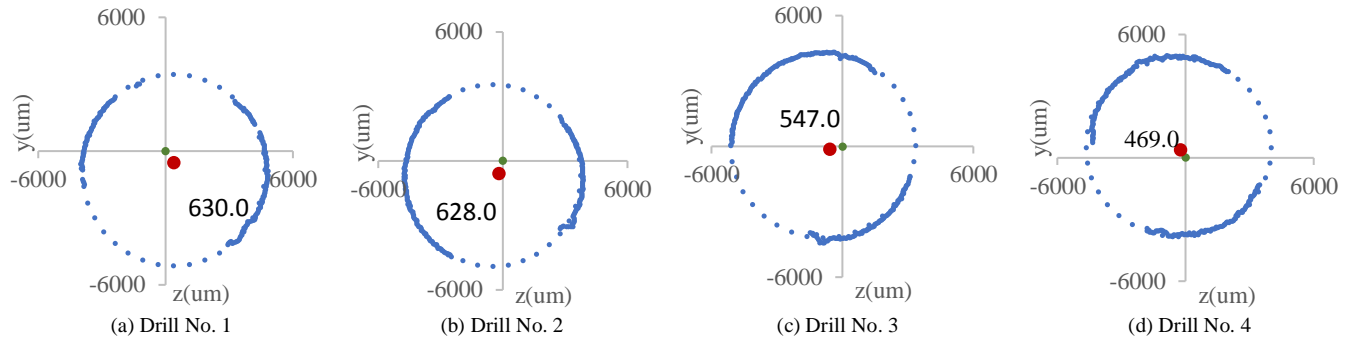


Fig. 23. Least-squares circle fitting for cross section. The points of cross section with maximum deviation are blue. its fitted center is red, and the reference center is green, the fit circle is blue dot.

According to Eq. (23), coaxiality error of drills is 2 times of radial distance from the center of cross sections on maximum axis deviation position to that of the reference position which is on the handle part. So, the desired cross sections were reconstructed by utilizing extracted blade back data in

accordance with Eq. (1), and their respective centers were calculated by using least-squares circle fitting method. As shown in Fig. 23, points of the positioned cross section with maximum deviations are blue, and its center is red, the fitting center of reference cross section is green.

Table IV
Measurement results for Drill No.1~4

Drill	Method	1 _{th} (mm)	2 _{th} (mm)	3 _{th} (mm)	4 _{th} (mm)	5 _{th} (mm)	6 _{th} (mm)	7 _{th} (mm)	8 _{th} (mm)	9 _{th} (mm)	10 _{th} (mm)	Average(mm)	Standard deviation
1	CMM	0.627	0.633	0.635	0.626	0.625	0.631	0.625	0.631	0.629	0.627	0.629	0.003
	Manual	0.790	0.559	0.675	0.576	0.681	0.671	0.574	0.702	0.691	0.624	0.643	0.052
	Ours	0.625	0.637	0.629	0.627	0.635	0.631	0.629	0.635	0.622	0.623	0.629	0.005
2	CMM	0.620	0.623	0.624	0.622	0.627	0.625	0.628	0.629	0.621	0.624	0.624	0.003
	Manual	0.672	0.681	0.629	0.643	0.619	0.642	0.640	0.553	0.547	0.652	0.628	0.043
	Ours	0.618	0.625	0.630	0.621	0.622	0.626	0.622	0.631	0.630	0.623	0.625	0.004
3	CMM	0.546	0.543	0.544	0.543	0.547	0.545	0.543	0.544	0.546	0.544	0.545	0.001
	Manual	0.578	0.551	0.563	0.609	0.553	0.540	0.543	0.573	0.539	0.492	0.554	0.029
	Ours	0.543	0.5524	0.546	0.549	0.550	0.551	0.544	0.552	0.539	0.540	0.547	0.005
4	CMM	0.465	0.462	0.467	0.469	0.468	0.470	0.466	0.472	0.469	0.468	0.468	0.003
	Manual	0.517	0.470	0.426	0.542	0.538	0.492	0.453	0.573	0.477	0.464	0.492	0.038
	Ours	0.468	0.467	0.463	0.473	0.469	0.466	0.465	0.467	0.472	0.475	0.469	0.004

During experiments, an ocean of tests have been carried out on various specifications of twist drills. Thereinto, ten times measurement results of 4 drills with 100mm in length and 10mm in diameter are listed in Table IV corresponding Fig. 20. Furthermore, manual method of V-type bracket plus dial meter and CMM method of ZEISS SPECTRUM were also adopted for comparing the accuracy and stability of measurements as shown in Fig. 24. It can be seen that our method performs a pleasurable result in accuracy and stability.

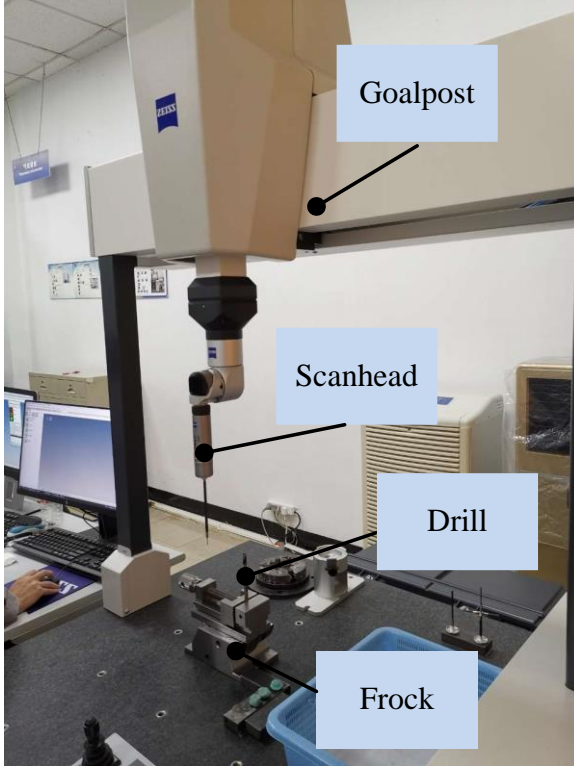


Fig. 24. CMM of ZEISS SPECTRUM.

E. Analysis of measurement uncertainty

In the system, measurement accuracy is mainly affected by the precision and resolution of core components such as rotary table, differential encoder, line structured light sensor and so on. Under the influence, measurement error is transferred from system calibration to data acquisition, and finally spreads to measurement results. For the rotating-based measurement mode, its basic principle is to drive objects rotating around turntable axis, collect external contour data under each angle, and measure coaxiality error of objects through cross section reconstruction. In other words, the actual axis is obtained by measuring the radius R . So specific factors are vital to measurement accuracy during data gathering. In the first place, two kinds of displacements may occur about the axis position including axial and radial displacement. Among them, the radial deviation will bring errors, while the axial deviation will not. Radically, the radial error is mainly introduced by turntable eccentricity and running accuracy. According to Table II, turntable eccentric is less than 5 μ m, so the uncertainty brought by which is 5 μ m recorded as Δc , and $\Delta c \leq 5 \mu$ m. On the other hand, the running angle error reacts worst when it occurs at the data acquiring moment, which generates the most deviation on the $O_w Z_w$ axis. The angel accuracy is 0.001°

shown in Table II, so the uncertainty of running accuracy is $\Delta \eta = R * (1 - \cos(0.001^\circ))$, $\Delta \eta \ll \Delta c$, so it can be neglected. Otherwise, the precision of the line structure sensor is 3 μ m as shown in Table I, so its uncertainty is denoted as Δz , and $\Delta z \leq 3 \mu$ m.

During calibration process, max system error occurs when the axis of rotating shaft is within light plane and generate maximum eccentricity, its uncertainty is denoted as $\Delta D = \Delta z + \Delta c$. In time of measurements, maximum systematic error occurs at the time that the center of drill cross section and the turntable axis are both within optical plane and meanwhile maximum eccentricity appears on the turntable, so the maximum deviation of measured point is $\Delta z_p = \Delta z + \Delta c$. That is to say the maximum deviation of measured radius $\Delta R = \Delta D + \Delta z_p + \Delta \eta$. Referring to the tolerance range of radial jump variable of drills, the tolerance range of coaxiality error is $C_s = 0.03 + 0.01 * (L / D_d)$. L and D_d are respectively the length and diameter of measured drills. The proportion of the uncertainty of R to the tolerance range of coaxiality error is ε as shown in Eq. (24):

$$\varepsilon = \frac{\Delta R_{\max}}{0.03 + 0.01 * (L / D_d)} \quad (24)$$

If the ratio is desired to be controlled within 20%, Eq. (25) must be derived:

$$\frac{R}{L} \leq 10 \quad (25)$$

This is fully compatible with the coaxiality error measurement requirements of most specifications of twist drills. Therefore, our method is accurate and efficient.

V. CONCLUSION

The surface of twist drill is complex, but its coaxiality error is an important quality standard. In this paper, a novel framework based on rotating mode is presented. The framework mainly includes four main components. In the calibration phase, following the calibration criterion from coarse to fine, best installation position and posture were obtained by using the three-degree-of-freedom cyclic calibration method, and the conversion parameter D between the two coordinate systems was obtained. During data acquiring, on one side twist drill rotates around the turntable axis in command of PLC, on the other side line structured light sensor collects contours data of drill surfaces triggered by encoder. Target region extraction is a key stage, a Gaussian mixture model algorithm based on local depth features was proposed to extract point cloud of blade back, and a statistical filter is used to exclude inevitable noise. In coaxiality error calculation phase, aiming at traditional time-consuming problem, an axis reconstruction method based on orthogonal synthesis of axisymmetric contours differences is proposed to estimate and locate the possible maximum axis deviation positions. Finally, least-squares circle fitting method is utilized to calculate reference axis and possible maximum deviation axes positions. In this way, coaxiality error is deviated. In order to avoid positioning error caused by the reconstruction from few contour lines, coaxiality error was calculated within a certain range. In addition, several other algorithms are tested to compare segmentation effect, and our algorithm is proved to

obtain an ideal target. During coaxiality error calculation experiments, drills with different bending degrees were examined. In the result, standard deviation of our method is kept within 0.005 that is close to 0.003 of CMM whose accuracy is 2 μm , the maximum deviation of the measurement results from CMM is maintained within 0.008 mm which is far less than that of the manual method 0.079 mm. This certifies that our method is not only accurate and stable, but also extremely suitable for industrial environment. On the side, system uncertainty is analyzed and evaluated for ascertaining suitable applications or system updating.

In the actual scenario test, it is noticed that the proposed system is not good enough for all scenes. Several factors such as turntable precision, encoder subdivision degree or sensor resolution play a crucial role in measurement accuracy. It is centrally embodied in axis calibration and data measurement. Furthermore, frock abrasion or platform jitter impress equipment stability. By now, several schemes could be considered to do, such as replacing with core components with higher resolution, adding seismic platform, substituting frocks and the like, so as to achieve an ideal accuracy and reliability.

ACKNOWLEDGMENT

This work is being supported by the National Key Research and Development Project of China under Grant No. 2020AAA0104001, the Zhejiang Lab. under Grant No. 2019KD0AD011005 and the Zhejiang Provincial Science and Technology Planning Key Project of China under Grant No. 2021C03129.

REFERENCES

- [1] ISO 1101. Geometrical product specifications (GPS) - geometrical tolerancing - tolerances of form, orientation, location and run-out. 2012.
- [2] U. Roy and Y. Xu, "Form and orientation tolerance analysis for cylindrical surfaces in computer-aided inspection," *Computers in Industry*, vol. 26, (2), pp. 127-134, 1995.
- [3] S. Zhang, "High-speed 3D shape measurement with structured light methods: A review," *Optics and Lasers in Engineering*, vol. 106, pp. 119-131, 2018.
- [4] X. Su and Q. Zhang, "Dynamic 3-D shape measurement method: A review," *Optics and Lasers in Engineering*, vol. 48, (2), pp. 191-204, 2010.
- [5] Z. H. Zhang, "Review of single-shot 3D shape measurement by phase calculation-based fringe projection techniques," *Optics and Lasers in Engineering*, vol. 50, (8), pp. 1097-1106, 2012.
- [6] S. Zhu and Y. Gao, "Noncontact 3-D Coordinate Measurement of Cross-Cutting Feature Points on the Surface of a Large-Scale Workpiece Based on the Machine Vision Method," *IEEE Transactions on Instrumentation and Measurement*, vol. 59, (7), pp. 1874-1887, 2010.
- [7] A. Fischer, "Angular-Dependent Radius Measurements at Rotating Objects Using Underdetermined Sensor Systems," *IEEE Transactions on Instrumentation and Measurement*, vol. 67, (2), pp. 425-430, 2018.
- [8] Z. Han et al, "A 3D measuring path planning strategy for intelligent CMMs based on an improved ant colony algorithm," *International Journal of Advanced Manufacturing Technology*, vol. 93, (1), pp. 1487-1497, 2017.
- [9] J. C. Rodríguez-Quinones et al, "Improve a 3D distance measurement accuracy in stereo vision systems using optimization methods' approach," *Opto-Electronics Review*, vol. 25, (1), pp. 24-32, 2017.
- [10] X. Chen et al, "Analytical solution of uncertainty with the GUM method for a dynamic stereo vision measurement system," *Optics Express*, vol. 29, (6), pp. 8967-8984, 2021.
- [11] R. Anchini et al, "A Comparison Between Stereo-Vision Techniques for the Reconstruction of 3-D Coordinates of Objects," *IEEE Transactions on Instrumentation and Measurement*, vol. 55, (5), pp. 1459-1466, 2006.
- [12] U. R. Dhond and J. K. Aggarwal, "Structure from stereo-a review," *IEEE Transactions on Systems, Man, and Cybernetics*, vol. 19, (6), pp. 1489-1510, 1989.
- [13] N. Lazaros, G. C. Sirakoulis and A. Gasteratos, "Review of Stereo Vision Algorithms: From Software to Hardware," *International Journal of Optomechatronics*, vol. 2, (4), pp. 435-462, 2008.
- [14] Y. Wang et al, "Review of surface profile measurement techniques based on optical interferometry," *Optics and Lasers in Engineering*, vol. 93, pp. 164-170, 2017.
- [15] A. Kolb et al, "Time-of-Flight Cameras in Computer Graphics," *Computer Graphics Forum*, vol. 29, (1), pp. 141-159, 2010.
- [16] C. Altuntas et al, "MEASUREMENT AND ANALYSIS OF GAIT BY USING A TIME-OF-FLIGHT CAMERA," *International Archives of the Photogrammetry, Remote Sensing and Spatial Information Sciences*, vol. XLI-B3, pp. 459-464, 2016.
- [17] P. Lavoie, D. Ionescu and E. M. Petriu, "3-D Object Model Recovery From 2-D Images Using Structured Light," *IEEE Transactions on Instrumentation and Measurement*, vol. 53, (2), pp. 437-443, 2004.
- [18] J. Salvi et al, "A state of the art in structured light patterns for surface profilometry," *Pattern Recognition*, vol. 43, (8), pp. 2666-2680, 2010.
- [19] X. Cao et al, "Defect detection method for rail surface based on line-structured light," *Measurement: Journal of the International Measurement Confederation*, vol. 159, pp. 107771, 2020.
- [20] Y. Xie, J. Tian and X. X. Zhu, "Linking Points With Labels in 3D: A Review of Point Cloud Semantic Segmentation," *IEEE Geoscience and Remote Sensing Magazine*, vol. 8, (4), pp. 38-59, 2020.
- [21] E. Grilli, F. Menna and F. Remondino, "A review of point clouds segmentation and classification algorithms," in *Conference on 3D Virtual Reconstruction and Visualization of Complex Architectures in*, 2017, pp. 339, 344.
- [22] Y. Guo et al, "Deep Learning for 3D Point Clouds: A Survey," *IEEE Transactions on Pattern Analysis and Machine Intelligence*, vol. PP, pp. 1-1, 2020.
- [23] A. D. Sappa and M. Devy, "Fast range image segmentation by an edge detection strategy," in *Proc. Third Int. Conf. 3-D Digital Imaging and Modeling*, 2001, pp. 292-299.
- [24] M. A. Wani and H. R. Arabnia, "Parallel edge-region-based segmentation algorithm targeted at reconfigurable multiring network," *J. Supercomputing*, vol. 25, no. 1, pp. 43-62, 2003.
- [25] J. Huang and C. - Menq, "Automatic data segmentation for geometric feature extraction from unorganized 3-D coordinate points," *IEEE Transactions on Robotics and Automation*, vol. 17, (3), pp. 268-279, 2001.
- [26] J.-E. Deschaud and F. Goulette, "A fast and accurate plane detection algorithm for large noisy point clouds using filtered normals and voxel growing," in *Proc. 3DPVT Int. Conf.*, 2010, pp. 1-8.
- [27] A.-V. Vo, L. Truong-Hong, D. F. Laefer, and M. Bertolotto, "Octree-based region growing for point cloud segmentation," *ISPRS J. Photogrammetry Remote Sensing*, vol. 104, pp. 88-100, 2015.
- [28] R. Hulik et al, "Continuous plane detection in point-cloud data based on 3D Hough Transform," *Journal of Visual Communication and Image Representation*, vol. 25, (1), pp. 86-97, 2014.
- [29] A. Nurunnabi, G. West and D. Belton, "Outlier detection and robust normal-curvature estimation in mobile laser scanning 3D point cloud data," *Pattern Recognition*, vol. 48, (4), pp. 1404-1419, 2015.
- [30] M. Shahzad, X. X. Zhu, and R. Bamler, "Facade structure reconstruction using spaceborne TomoSAR point clouds," in *2012 IEEE Int. Geoscience and Remote Sensing Symp.*, pp. 467-470.
- [31] X. X. Zhu and M. Shahzad, "Facade reconstruction using multiview spaceborne TomoSAR point clouds," *IEEE Trans. Geosci. Remote Sens.*, vol. 52, no. 6, pp. 3541-3552, 2014.
- [32] M. Shahzad, M. Schmitt, and X. X. Zhu, "Segmentation and crown parameter extraction of individual trees in an airborne TomoSAR point cloud," *Int. Archives Photogrammetry, Remote Sensing Spatial Inform. Sci.*, vol. 40, pp. 205-209, 2015.
- [33] M. Schmitt, M. Shahzad, and X. X. Zhu, "Reconstruction of individual trees from multi-aspect TomoSAR data," *Remote Sensing Environment*, vol. 165, pp. 175-185, 2015.
- [34] A. Sampath and J. Shan, "Segmentation and reconstruction of polyhedral building roofs from aerial lidar point clouds," *IEEE Trans. Geosci. Remote Sens.*, vol. 48, no. 3, pp. 1554-1567, 2010.
- [35] Y. Xu, W. Yao, S. Tutas, L. Hoegner, and U. Stilla, "Unsupervised segmentation of point clouds from buildings using hierarchical clustering based on gestalt principles," *IEEE J. Sel. Topics Appl. Earth Observ. Remote Sens.*, no. 99, pp. 1-17, 2018.

- [36] Z. Chai et al, "Non-contact measurement method of coaxiality for the compound gear shaft composed of bevel gear and spline," *Measurement: Journal of the International Measurement Confederation*, vol. 168, pp. 108453, 2021.
- [37] Y. Pei, H. Xie and Q. Tan, "A non-contact high precision measuring method for the radial runout of cylindrical gear tooth profile," *Mechanical Systems and Signal Processing*, vol. 138, pp. 106543, 2020.
- [38] Y. Zhang et al, "A concentricity measurement method for large forgings based on laser ranging principle," *Measurement: Journal of the International Measurement Confederation*, vol. 147, pp. 106838, 2019.
- [39] H. Li et al, "New Measurement Method for Spline Shaft Rolling Performance Evaluation using Laser Displacement Sensor," *Chinese Journal of Mechanical Engineering*, vol. 31, (1), pp. 1-9, 2018.



Ailing Cheng was born in Handan, Hebei Province, China in 1982. She received her B.S. degree in automation engineering from Northeastern University in 2005. From 2005 to 2008, she has pursued her master degree at Information Science and Engineering Department, Northeastern University, Hangzhou, Zhejiang Province, China.

She is currently studying for a doctor's degree in computer science engineering at Zhejiang University of Technology, Hangzhou, Zhejiang Province, China. Her research interests include computer vision, three-dimensional object detection, identification and measurement.



Jiaojiao Ye is currently an AI algorithm engineer at Intelligent Center at Zhejiang Lab. She works on AI algorithms, including distributed training for large-scale DL algorithm, Nas etc, serving for Tianshu AI open source platform.

From 2016 to 2020, she has pursued her master degree at Electrical and Computer Engineering Department, Technical University of Munich, Germany. During that time, she was once a part of the AI research Lab at Volkswagen Data Lab, working on Conditional VAE and Probabilistic Movement Primitives on Human-Robot-Interaction. Her major research interests include reinforcement learning, image representation and synthesis, and ML in robotics.



Fei Yang was born in Zhenjiang, Jiangsu Province, China in 1988. He received the B.S. and M.S. degree in computer science from Shanghai Jiao Tong University, in 2011 and 2014, and the Ph.D. degree in computer science from Eindhoven University of Technology, the Netherlands, in 2018. From 2019 to 2020, He worked as a research fellow at Cyber Security Lab in the department of computer science and engineering in Nanyang Technological University, Singapore. Since 2020, he works at Zhejiang Lab as an advanced research specialist.

His major research interests include deep learning framework, deep learning algorithms and distributed learning techniques. He is the technical director of the Tianshu AI open source platform.



Shufang Lu was born in Hangzhou, Zhejiang Province, China in 1984. She received her B.S. degree in software engineering from Wuhan University, Wuhan, China, in 2007, and Ph.D. degrees in computer science and technology from Zhejiang University, Hangzhou, Zhejiang Province, China, in 2013.

Since 2013, she works in the Laboratory of Graphics & Image Processing, College of Computer Science and Technology, Zhejiang University of Technology, Hangzhou, Zhejiang Province, China. Since 2013, she has been an assistant professor. She is the author of more than 20 articles. Her research interests include non-photorealistic rendering, image and video processing.



Fei Gao was born in Linshui, Sichuan Province, China in 1974. He received the B.S. degree in mechanical engineering from the Zhejiang University, Hangzhou, China, in 1998 and the Ph.D. degree in mechanical engineering from Zhejiang University, Hangzhou, Zhejiang Province, China, in 2004.

Since 2004, He works in the Laboratory of Graphics & Image Processing, College of Computer Science and Technology, Zhejiang University of Technology, Hangzhou, Zhejiang Province, China. From 2004 to 2006, he was a Lecturer. From 2006 to 2011, he was an Associate Professor. Since 2011, he is a Professor and the Director of the Laboratory of Graphics & Image Processing. He is the author of a book, more than 90 articles, and more than 70 inventions. His research interests include visual perception and understanding, pattern recognition, object tracking and background modeling.